Supporting Information for:

Effective Entanglement and Constraint Release in Deformed Polymer Melts

Lin-Feng Wu[†], Long-Fei Mao[†], Zhe Wang[†,*]

†Department of Engineering Physics and Key Laboratory of Particle and Radiation Imaging

(Tsinghua University) of Ministry of Education, Tsinghua University, Beijing 100084, China

*zwang2017@mail.tsinghua.edu.cn

CONTENTS

S1. Molecular dynamics simulation

The extensively used Kremer-Grest bead-spring model[1] is employed to model the entangled polymer melts. All beads interact with the purely repulsive Lennard-Jones (LJ) potential, commonly referred to as the Weeks-Chandler-Andersen (WCA) potential:

$$U_{\text{WCA}}(r) = \begin{cases} 4\varepsilon\left[\left(\frac{\sigma}{r}\right)^{12} - \left(\frac{\sigma}{r}\right)^{6}\right] + \varepsilon & r < 2^{\frac{1}{6}}\sigma \\ 0 & r \geq 2^{\frac{1}{6}}\sigma \end{cases}. \quad \text{(S1-1)}$$

where r is the distance between two beads, σ is the effective diameter, and ε denotes the strength of the LJ interaction. Attractive finitely extensible nonlinear elastic (FENE) potential is adopted to describe the interaction of covalent bonds:

$$U_{\text{FENE}}(r) = \begin{cases} -\frac{1}{2}kR_0^2 \ln\left[1 - \left(\frac{r}{R_0}\right)^2\right], & r < R_0 \\ \infty, & r \geq R_0 \end{cases}. \quad \text{(S1-2)}$$

where $k = 30\varepsilon/\sigma^2$ and $R_0 = 1.5\sigma$. All physical quantities are expressed in reduced Lennard-Jones units: The units of length, energy, and time are respectively represented by σ, ε, and $\tau_0 = \sigma\sqrt{m/\varepsilon}$. The mass of monomer is set to $m = 1$.

The system consists of $M_c = 250$ chains with a fixed number density $\rho = M_c N/V = 0.85\sigma^{-3}$, where N is the number of monomers contained in one chain, and V is the volume of the simulation box. In this work, three values of N are adopted: $N = 700, 1000,$ and 1500. All of these melts are well entangled.

Well equilibrated initial configurations are crucial for MD. Due to the high ρ of the system, directly generating such a system is challenging, since the close proximity of monomers may lead to excessively high system energy, resulting in the collapse of the system. Therefore, we initially generate a system with $\rho = 0.001\sigma^{-3}$ within a cubic volume and subsequently adjust the number density to $\rho = 0.85\sigma^{-3}$ through compression after resolving overlap.

Two tube-model parameters, the equilibrium number of monomers per entanglement N_e and Rouse time of an entangled strand τ_e are respectively set to $N_e = 60$ and $\tau_e = 3290$ as suggested by Cao and Likhtman.[2] Some alternative methods, such as PPA,[3] yield $N_e = 85$, slightly larger than the value we adopted. However, earlier finding[4] suggests that the results of Cao and Likhtman are more consistent with rheology experiment. Moreover, the small difference in the value of N_e is not expected to significantly impact our main conclusions. The Rouse time of the whole chain τ_R is determined from the relation $\tau_R = (N/N_e)^2\tau_e$.

We used LAMMPS package[5] to simulate the polymer system with a time step $\delta t = 0.01\tau_0$. A Monte Carlo bond-swap algorithm is implemented to accelerate the equilibration of the system. Then, an additional run, about $2\tau_R$, is performed to further equilibrate the system.
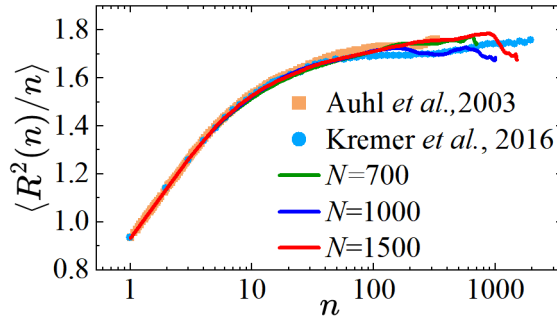

Figure S1. Results of mean square internal distance $\langle R^2(n)/n \rangle$ for various chain lengths are compared with previous results.[6,7]

We have examined several quantities to assess whether the system is well equilibrated. A commonly-used quantity is the mean square internal distance $\langle R^2(|i-j|)\rangle$. The rescaled $\langle R^2(n)/n \rangle$ $(n = |i-j|)$ is expected to reach a plateau as N increases. As illustrated in Figure S1, the simulation results indeed align with expectations, eventually reaching a plateau that is highly consistent with previous simulations by other researchers.[6,7] We also checked the radius of gyration and the static single-chain structure factor, and compared these with previous

results.[4,8]

The equilibrated polymer melts are strained by isochoric uniaxial elongation at an initial Rouse Weissenberg number $Wi_{R,i} = \tau_R \dot{\varepsilon}_i = 40$, where $\dot{\varepsilon}_i$ is the initial strain rate. The deformation is stopped once the desired stretch ratio λ is achieved. Here, the values of λ we adopt are 1.8, 3, and 5. The stress-strain curves with the system of $N = 1000$ for three $\lambda = 1.8, 3, 5$ during stretch are illustrated in Figure S2. Then, the strained system undergoes relaxation up to $\sim\tau_d$ (τ_d is the disengagement time in the tube model) with a Langevin thermostat.
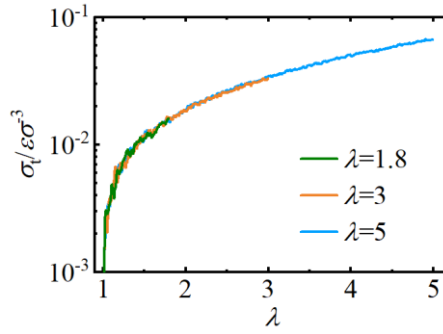

Figure S2. The stress-strain data during stretch for $\lambda = 1.8, 3, 5$ with the system of $N = 1000$.

In order to maintain consistency with experimental conditions, our simulations employed a constant engineering strain rate rather than a constant true strain rate. Therefore, the true strain rate of the simulation decreases gradually during the stretching process. However, even at the maximum elongation ratio $\lambda = 5$, the Rouse Weissenberg number Wi_R remains significantly greater than 1. Therefore, our simulation can still be considered as a step-strain deformation. To validate the time-strain separation in step strain, we employed three damping functions to superpose the stress relaxation data of the system with $N = 1000$: the classical network stress-strain relation $h(\lambda) = \lambda^2 - \lambda^{-1}$, the Doi-Edwards damping function,[9] and the Rubinstein-

Panyukov damping function $h_{RP}(\lambda) = (\lambda^2 - \lambda^{-1})/(\lambda - \lambda^{0.5} + 1)$.[10] As seen from Figure S3,

the Rubinstein-Panyukov damping functions effectively superpose the stress data, validating

the time-strain separation in our simulations. To maintain consistency with the SANS analysis,

the average stretch ratio of chains $\bar{\lambda}_c$, which is slightly smaller than the stretch ratio of the melt

λ, is utilized to calculate the damping function. Here, the values of $\bar{\lambda}_c$ are 1.76, 2.82, and 4.52

for $\lambda = 1.8, 3$ and 5, respectively. In fact, both λ and $\bar{\lambda}_c$ well superimpose the stress data
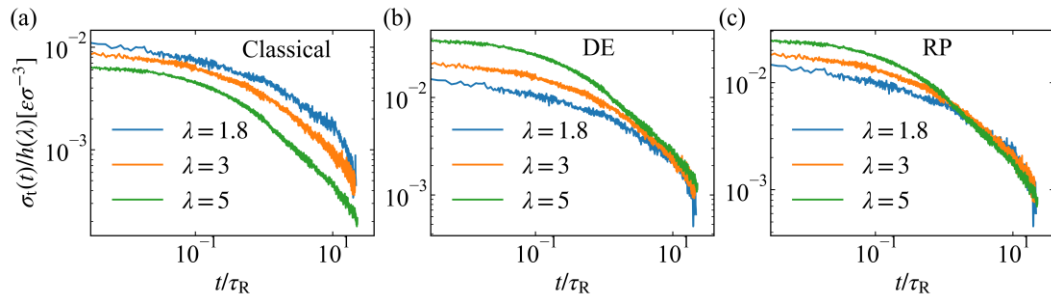
with $h_{RP}(\lambda)$.

Figure S3. $\sigma_t(t)/h(\lambda)$ from (a) classical stress-strain relation, (b) Doi-Edwards damping function, and (c) Rubinstein-Panyukov damping function.

S2. Experiment

In this work, we re-analyze the Small-Angle Neutron Scattering (SANS) spectra of a set of polystyrene melts that we have published in [*Macromolecules* 2018, 51, 9011-9018]. In this section, we will briefly introduce the sample and experiment.
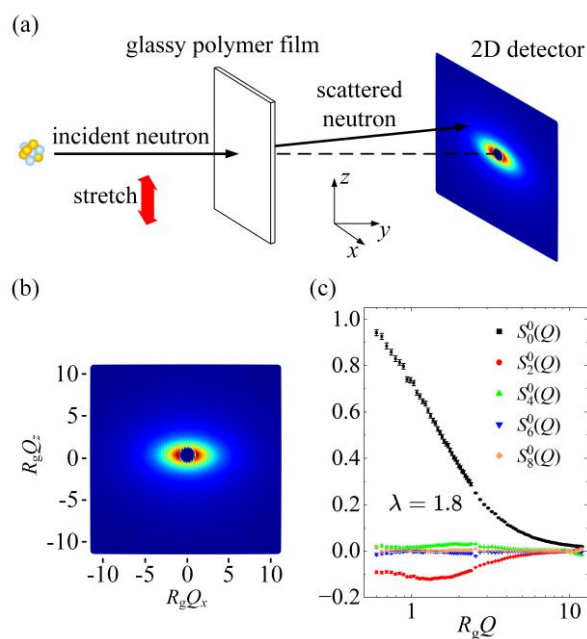

Figure S4. (a) Illustration of the SANS experiment on the uniaxially stretched polymers. (b) 2D SANS spectrum of the sample immediately after stretching to $\lambda = 1.8$. (c) Selected spherical harmonic expansion cofficients for the spectrum shown in panel b.

The experimental melt is a mixture of protonated and deuterated polystyrene homopolymers with a d/h ratio of 10/90 (h-PS: $m_w = 197$ kg/mol, $m_w/m_n = 1.01$; d-PS: $m_w = 213$ kg/mol, $m_w/m_n = 1.06$, m_w and m_n are weight-average and number-average molecular weights, respectively). The isotropic samples were uniaxially stretched to $\lambda = 1.8$ at 124 °C with a constant crosshead velocity $v = 8l_0/\tau_R$ first, where l_0 is the original length of the sample, and τ_R is the Rouse time calculated by the Osaki formula [$\tau_R = (6m_w\eta/\pi^2\rho RT)(1.5m_e/m_w)^2$], where η is the zero-shear viscosity, m_e is the entanglement molecular weight, ρ is the mass density of the

polymer, and R is the universal gas constant. The stretched samples were allowed to relax for different amount of time at 124 °C at the constant strain and then quenched to the glassy state for the *ex-situ* SANS measurement.

Figure S4a gives an illustration of the SANS experiment. Figure S4b gives the SANS spectrum of the sample immediately after stretching to $\lambda = 1.8$. The spectrum is highly anisotropic. In our previous study,[11] we show that such spectrum $S(\boldsymbol{Q})$ can be expanded by spherical harmonics as:

$$S(\boldsymbol{Q}) = \sum_{l:\text{even}} S_l^0(Q) Y_l^0(\widehat{\boldsymbol{Q}}). \text{ (S2-1)}$$

where $Y_l^0(\boldsymbol{\Omega})$ is the real spherical harmonic function and $S_l^0(Q)$ is the corresponding coefficient. In the SANS experiment shown in Figure S4a, the scattering intensity given by the 2D detector is the cross section of $S(\boldsymbol{Q})$ in the $x - z$ plane, namely, $S(Q_x, Q_y = 0, Q_z)$, or equivalently, $S(Q, \theta, \phi = 0)$. One can obtain $S_l^0(Q)$ from the measured SANS spectrum through the following relation:[11]

$$S_l^0(Q) = \frac{1}{2} \int_0^\pi S(Q, \theta, \phi = 0) Y_l^0(\theta) \sin \theta \, d\theta. \text{ (S2-2)}$$

In Figure S4c we give the first 5 coefficients.

S3. SANS model and data analysis

In this section, we give the details of the SANS model and data analysis. Our SANS model is based on the nonaffine tube model (NTM) proposed by Rubinstein and Panyukov.[10] In this model, the tube confinement is modeled by a set of virtual chains acting on the test chain, as illustrated in Figure S5. The NTM points out that for entangled polymer melts under strong elongation, there is a nonaffine monomer separation $N_{aff} = \lambda N_e$, where λ is the stretch ratio and N_e is the PP step length. For monomers i and j in one deformed chain, their displacement undergoes affine deformation if $|i - j| > N_{aff}$, while nonaffinity emerges at $|i - j| < N_{aff}$. N_{aff} is also the separation between two adjacent virtual "crosslinks" that connect to virtual chains, as illustrated in Figure S5.
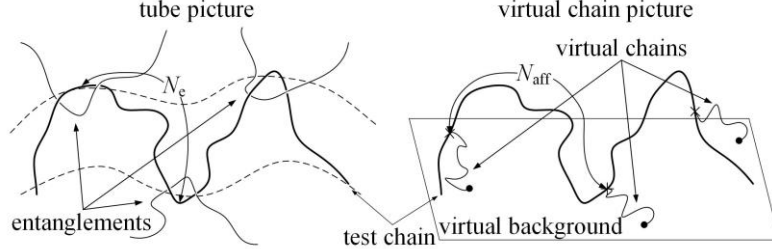

Figure S5. Illustration of the nonaffine tube model.

In our picture, the length of PP step of a deformed chain is determined by the separation between two adjacent effective entanglements $N_{ee} = N/(Z_{ee} + 1)$, where N is the monomer number in one chain, and Z_{ee} is the average number of effective entanglements per chain. In contrast, the ineffective kinks and relaxed neighboring chains give no orientational constraint. Thus, according to the NTM, the nonaffine monomer separation can be written as $N_{aff} = \lambda N_{ee}$. To avoid the unphysical situation of $N_{aff} > N$ at large λ, we practically correct N_{aff} as:

$$N_{aff} = N\left[1 - \exp\left(-\frac{\lambda N_{ee}}{N}\right)\right] = N\left[1 - \exp\left(-\frac{\lambda}{Z_{ee}+1}\right)\right]. \text{ (S3-1)}$$

For $|i - j| \geq N_{\text{aff}}$, the deformation is affine. Therefore, the probability $\phi(i,j,\boldsymbol{r})$ of finding monomer j at distance $\boldsymbol{r}$ from monomer i is given by an affine Gaussian form:

$$\phi(i,j,\boldsymbol{r}) = \left(\frac{3}{2\pi|i-j|b^2}\right)^{3/2} \exp\left[-\frac{3}{2|i-j|b^2}\left(\lambda_{\text{M}}r_x^2 + \lambda_{\text{M}}r_y^2 + \frac{r_z^2}{\lambda_{\text{M}}^2}\right)\right], |i - j| \geq N_{\text{aff}}. \text{ (S3-2)}$$

where b is the bond length, the subscript "M" denotes model parameters. For $|i - j| < N_{\text{aff}}$, the pair distance $\boldsymbol{r}$ is no longer affinely distributed. In this case, monomers i and j are within a strand between two adjacent virtual crosslinks. Their distribution depends on the end-to-end vector $\boldsymbol{R}_{\text{s}}$ of such strand. This conditional probability $\phi(i,j,\boldsymbol{r}|\boldsymbol{R}_{\text{s}})$, which gives the probability that monomers i and j are separated by $\boldsymbol{r}$ under the condition that the strand ends are separated by $\boldsymbol{R}_{\text{s}}$, can be modeled by a bivariate Gaussian form:[12]

$$\phi(i,j,\boldsymbol{r}|\boldsymbol{R}_{\text{s}}) = \left[\frac{\beta^2}{\pi w_{ij}(1-w_{ij})}\right]^{3/2} \exp\left[-\frac{\beta^2}{w_{ij}(1-w_{ij})}\left(\boldsymbol{r} - w_{ij}\boldsymbol{R}_{\text{s}}\right)^2\right]. \text{ (S3-3)}$$

where $\beta^2 = 3/2N_{\text{aff}}b^2$, and $w_{ij} = |i - j|/N_{\text{aff}}$. Notice that at very large elongations, the local chain segment can be straightened, and this bivariate Gaussian form will fail. Then, considering that $\boldsymbol{R}_{\text{s}}$ is affinely distributed, we can write down that:

$$\phi(i,j,\boldsymbol{r}) = \int \phi(i,j,\boldsymbol{r}|\boldsymbol{R}_{\text{s}})\phi(\boldsymbol{R}_{\text{s}},\lambda)\text{d}\boldsymbol{R}_{\text{s}}, \quad |i - j| < N_{\text{aff}}. \text{ (S3-4)}$$

where $\phi(\boldsymbol{R}_{\text{s}},\lambda)$ is the affine distribution:

$$\phi(\boldsymbol{R}_{\text{s}},\lambda) = \left(\frac{\beta^2}{\pi}\right)^{3/2} \exp\left[-\beta^2\left(\lambda_{\text{M}}R_{\text{s},x}^2 + \lambda_{\text{M}}R_{\text{s},y}^2 + \frac{R_{\text{s},z}^2}{\lambda_{\text{M}}^2}\right)\right]. \text{ (S3-5)}$$

Combining the above two equations, we can obtain the pair distribution for $|i - j| < N_{\text{aff}}$:

$$\phi(i,j,\boldsymbol{r}) = \left(\frac{\beta^2}{\pi w_{ij}}\right)^{3/2} \sqrt{\frac{1}{\left(w_{ij}/\lambda_{\text{M}}+1-w_{ij}\right)^2\left(w_{ij}\lambda_{\text{M}}^2+1-w_{ij}\right)}} \times$$
$$\exp\left[-\frac{\beta^2}{w_{ij}}\left(\frac{r_x^2+r_y^2}{w_{ij}/\lambda_{\text{M}}+1-w_{ij}} + \frac{r_z^2}{w_{ij}\lambda_{\text{M}}^2+1-w_{ij}}\right)\right], |i - j| < N_{\text{aff}} \quad . \text{ (S3-6)}$$

Now, we obtain the full form of $\phi(i,j,\boldsymbol{r})$ based on the idea of NTM.

SANS directly measures the structure factor $S(\boldsymbol{Q})$, rather than $\phi(i,j,\boldsymbol{r})$. These two quantities are connected by the pair distribution function $g(\boldsymbol{r})$ as follows:[13]

$$g(r) = \frac{1}{N^2} \sum_{i,j}^{N} \phi(i,j,\boldsymbol{r}), \ S(\boldsymbol{Q}) = \int g(\boldsymbol{r}) \exp(-i\boldsymbol{Q} \cdot \boldsymbol{r}) \, d\boldsymbol{r}. \ \text{(S3-7)}$$

For elongated SANS spectra, it can be expanded by spherical harmonics as:[11]

$$S(\boldsymbol{Q}) = \sum_{l:\text{even}} S_l^0(Q) Y_l^0(\widehat{\boldsymbol{Q}}). \ \text{(S3-8)}$$

where $Y_l^0(\boldsymbol{\Omega})$ is the real spherical harmonic function. Similarly, $\phi(i,j,\boldsymbol{r})$ and $g(\boldsymbol{r})$ can also be expanded by spherical harmonics:

$$\phi(i,j,\boldsymbol{r}) = \sum_{l:\text{even}} \phi_l^0(i,j,r) Y_l^0(\hat{\boldsymbol{r}}), \ g(\boldsymbol{r}) = \sum_{l:\text{even}} g_l^0(r) Y_l^0(\hat{\boldsymbol{r}}). \ \text{(S3-9)}$$

Knowing $\phi_l^0(i,j,r)$, $S_l^0(Q)$ can be calculated as follows:[13]

$$g_l^0(r) = \frac{1}{N^2} \int_0^N di \int_0^N dj \phi_l^0(i,j,r). \ \text{(S3-10)}$$

$$S_l^0(Q) = i^l 4\pi \int_0^\infty g_l^0(r) J_l(Qr) r^2 dr. \ \text{(S3-11)}$$

where $J_l(x)$ is the lth order spherical Bessel function. With above equations, we can obtain the theoretical $S_2^0(Q)$. Notice that in this model, there are only two fitting parameters, the stretch ratio λ_M and the average number of effective entanglements per chain $Z_{ee,M}$ ($Z_{ee,M}$ is contained in N_{aff}, as shown in eq. S3-1). According to the NTM, the tensile stress is given by:

$$\sigma_{t,M} = \frac{M_c}{V} kT (Z_{ee,M} + 1) \left(\lambda_M - \lambda_M^{-1} + \lambda_M^{1/2} - \lambda_M^{-1/2} \right). \ \text{(S3-12)}$$

where M_c/V gives the chain number density. If we assume that the chain is formed by strands connected by virtual crosslinks, we can employ the expression for network to calculate the tensile stress:

$$\sigma_{t,M} = \frac{M_c}{V} kT (Z_{ee,M} + 1) (\lambda_M - \lambda_M^{-2}). \ \text{(S3-13)}$$

For our samples and simulation data, above two equations give very similar results on the relaxation of normalized stress.

S4. Comparison between simulation and experiment

Here, we compare the relaxation processes between the simulated melt with $N = 1000$ and $\lambda = 1.8$ and the polystyrene sample due to their comparable entanglements and flow condition. Firstly, regarding the decay of the effective entanglements which is our primary concern, it can be observed from Figure S6a that both experimental and simulated results exhibit similar trends, displaying a clear -1/2 power law for $t \in [1\tau_R, 10\tau_R]$. We also compare the relaxation of $S_2^0(Q)$. As depicted in Figure S6b, at $t = 0\tau_R$, there is a nice agreement between the experimental and simulation results, and the subsequent relaxation rates are also quite similar. These consistent results indicate that our simulation and analysis capture the physical characteristics of entangled polymers effectively.
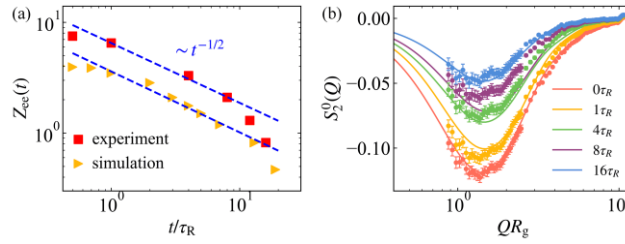

Figure S6. (a) The relaxation of the effective entanglements $Z_{ee}(t)$ and (b) $S_2^0(Q)$ (lines: simulation, symbols: experiments) after a step-strain of $\lambda = 1.8$ for experiments and simulation system of $N = 1000$.

S5. Tube segment survival probability

The tube segment survival probability $\Phi(l,t)$ gives the probability that the segment containing monomer l is still in the original tube at time t. For the relaxation after a strong step elongation, the classic tube model points out that the chain will firstly retract to its equilibrium length within $t < \tau_{\mathrm{ppr}}$ where τ_{ppr} is the characteristic time of retraction. Then, the orientation relaxation takes place through reptation. If considering the CR effect and modeling it by the decay of effective entanglements, we write down $\Phi(l,t)$ for $t \geq \tau_{\mathrm{ppr}}$ as:

$$\Phi(l,t) = \psi(t - \tau_{\mathrm{ppr}})\left[\frac{Z_{\mathrm{ee}}(t)}{Z_{\mathrm{ee}}(\tau_{\mathrm{ppr}})}\right], \text{for } t \geq \tau_{\mathrm{ppr}}, \text{ (S5-1)}$$

where $\psi(l,t) = \sum_{p:\mathrm{odd}}(4/p\pi)\sin(p\pi l/N)\exp(-p^2 t/\tau_{\mathrm{d}})$ is the equilibrium tube survival probability deduced from single-chain effects.
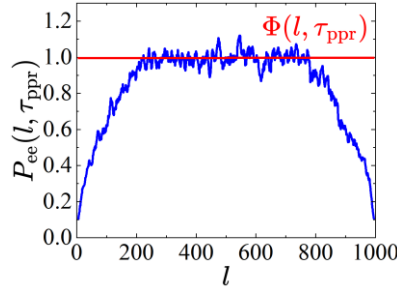

Figure S7. Comparison between $P_{\mathrm{ee}}(l,\tau_{\mathrm{ppr}})$ (blue line) and $\Phi(l,\tau_{\mathrm{ppr}})$ (red line). The values of $P_{\mathrm{ee}}(l,\tau_{\mathrm{ppr}})$ are lower near the chain ends due to the "dangling ends".

In our picture, the statistical distribution of effective entanglements $P_{\mathrm{ee}}(l,t)$ directly gives an evaluation of the tube segment survival probability. However, before comparing $P_{\mathrm{ee}}(l,t)$ with $\Phi(l,t)$ given by eq. S5-1, one needs to consider the "dangling-end effect". At the $t = \tau_{\mathrm{ppr}}$ moment, $\Phi(l,t = \tau_{\mathrm{ppr}})$ equals to 1 in the whole range of l. In contrast, the profile of $P_{\mathrm{ee}}(l,t = \tau_{\mathrm{ppr}})$ exhibits lower values when l is close to 1 or N due to the dangling chain ends. Figure S7 compares $P_{\mathrm{ee}}(l,t = \tau_{\mathrm{ppr}})$ and $\Phi(l,t = \tau_{\mathrm{ppr}})$, and this effect is clearly seen.

11

To correct this effect, we perform the following analysis.

At $t = \tau_{\mathrm{ppr}}$, $\Phi(l, t = \tau_{\mathrm{ppr}}) = 1$, which means that the average positions of the effective entanglements are uniformly distributed along the PP. The average interval between adjacent effective entanglements is $l_{\mathrm{dis}} = N/[Z_{\mathrm{ee}}(\tau_{\mathrm{ppr}}) + 1]$. Thus, the distribution of average positions of effective entanglements on the PP can be expressed as a series of δ functions, as illustrated in Figure S8a:

$$\delta_{\mathrm{ee}}(l) = \begin{cases} 1, & l = kl_{\mathrm{dis}}, k = 1, 2, \cdots, Z_{\mathrm{ee}}(\tau_{\mathrm{ppr}}) \\ 0, & \text{others} \end{cases} \quad \text{(S5-2)}$$

Note that the entanglements can "slip" along the PP before release, which smears out the above distribution. This effect can be taken into account by convoluting the distribution function with a Gaussian distribution. The standard deviation of this Gaussian function, representing the random displacement of the entanglement along PP, is tentatively set to l_{dis}. Here, we denote this Gaussian distribution by $K(l, l_{\mathrm{dis}})$. Figure S8c shows $\delta_{\mathrm{ee}}(l) * K(l, l_{\mathrm{dis}})$. It is seen that the convolution nicely describes the profile of $P_{\mathrm{ee}}(l, t)$ at $t = \tau_{\mathrm{ppr}}$. For moments at $t > \tau_{\mathrm{ppr}}$, $\Phi(l, t)$ can be regarded as the superposition of a series of δ functions. Therefore, we use the convolution $\Phi(l, t) * K(l, l_{\mathrm{dis}})$ as the theoretical result of the tube survival probability to correct the combined effect of dangling ends and slippery entanglements.
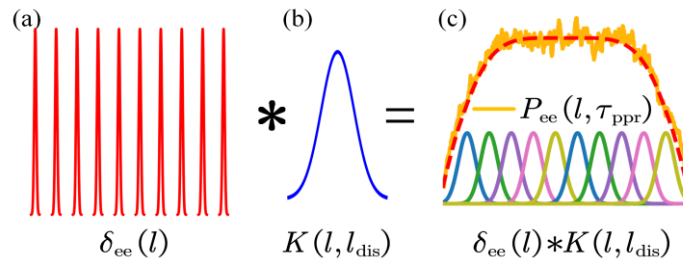

Figure S8. The convolution of $\delta_{\mathrm{ee}}(l)$ (a) with $K(l, l_{\mathrm{dis}})$ (b) yields the result depicted in (c). As seen in panel (c), the corrected result (red dashed line) exhibits good consistency with $P_{\mathrm{ee}}(l, \tau_{\mathrm{ppr}})$ (yellow solid line).

REFERENCES

(1) Kremer, K.; Grest, G. S. Dynamics of entangled linear polymer melts: A molecular-dynamics simulation. *J. Chem. Phys.* **1990**, *92*, 5057-5086.

(2) Cao, J.; Likhtman, A. E. Simulating Startup Shear of Entangled Polymer Melts. *ACS Macro Lett.* **2015**, *4*, 1376-1381.

(3) Everaers, R.; Sukumaran, S. K.; Grest, G. S.; Svaneborg, C.; Sivasubramanian, A.; Kremer, K. Rheology and Microscopic Topology of Entangled Polymeric Liquids. *Science* **2004**, *303*, 823-826.

(4) Xu, W.-S.; Carrillo, J.-M. Y.; Lam, C. N.; Sumpter, B. G.; Wang, Y. Molecular Dynamics Investigation of the Relaxation Mechanism of Entangled Polymers after a Large Step Deformation. *ACS Macro Lett.* **2018**, *7*, 190-195.

(5) Thompson, A. P.; Aktulga, H. M.; Berger, R.; Bolintineanu, D. S.; Brown, W. M.; Crozier, P. S.; In 'T Veld, P. J.; Kohlmeyer, A.; Moore, S. G.; Nguyen, T. D.; et al. LAMMPS - a flexible simulation tool for particle-based materials modeling at the atomic, meso, and continuum scales. *Comput. Phys. Commun.* **2022**, *271*, 108171.

(6) Hsu, H.-P.; Kremer, K. Static and Dynamic Properties of Large Polymer Melts in Equilibrium. *J. Chem. Phys.* **2016**, *144*, 154907.

(7) Auhl, R.; Everaers, R.; Grest, G. S.; Kremer, K.; Plimpton, S. J. Equilibration of long chain polymer melts in computer simulations. *J. Chem. Phys.* **2003**, *119*, 12718-12728.

(8) Lam, C. N.; Xu, W.-S.; Chen, W.-R.; Wang, Z.; Stanley, C. B.; Carrillo, J.-M. Y.; Uhrig, D.; Wang, W.; Hong, K.; Liu, Y.; et al. Scaling Behavior of Anisotropy Relaxation in Deformed Polymers. *Phys. Rev. Lett.* **2018**, *121*, 117801.

(9) Doi, M.; Edwards, S. F. *The theory of polymer dynamics*; Clarendon: Oxford, England, 1986.

(10) Rubinstein, M.; Panyukov, S. Nonaffine Deformation and Elasticity of Polymer Networks. *Macromolecules* **1997**, *30*, 8036-8044.

(11) Wang, Z.; Lam, C. N.; Chen, W.-R.; Wang, W.; Liu, J.; Liu, Y.; Porcar, L.; Stanley, C. B.; Zhao, Z.; Hong, K.; Wang, Y. Fingerprinting Molecular Relaxation in Deformed Polymers. *Phys. Rev. X* **2017**, *7*, 031003.

(12) Ullman, R. Small angle neutron scattering from polymer networks. *J. Chem. Phys.* **1979**, *71*, 436-449.

(13) Wang, Z.-Y.; Kong, D.; Yang, L.; Ma, H.; Su, F.; Ito, K.; Liu, Y.; Wang, X.; Wang, Z. Analysis of Small-Angle Neutron Scattering Spectra from Deformed Polymers with the Spherical Harmonic Expansion Method and a Network Model. *Macromolecules* **2018**, *51*, 9011-9018.